

Formation of Amorphous Carbon Multi-Walled Nanotubes from Random Initial Configurations

Chinonso Ugwumadu,* Rajendra Thapa, Yahya Al-Majali, Jason Trembly, and D. A. Drabold*

Amorphous carbon nanotubes (a-CNT) with up to four walls and sizes ranging from 200 to 3200 atoms have been simulated, starting from initial random configurations and using the Gaussian Approximation Potential. The important variables (like density, height, and diameter) required to successfully simulate a-CNTs were predicted with the machine learning random forest technique. The width of the a-CNT models ranged between 0.55–2 nm with an average inter-wall spacing of 0.31 nm. The topological defects in a-CNTs were analyzed and new defect configurations were observed. The electronic density of states and localization in these phases were discussed and delocalized electrons in the π subspace were identified as an important factor for inter-layer cohesion. Spatial projection of the electronic conductivity favors axial transport along connecting hexagons, while non-hexagonal parts of the network either hinder or bifurcate the electronic transport. A vibrational density of states was calculated and is potentially an experimentally comparable fingerprint of the material. The appearance of a low-frequency radial breathing mode was discussed and the thermal conductivity at 300 K was estimated using the Green-Kubo formula.

nanotubes (CNT) have been the focus of intense research with a range of applications in nano-scale engineering and electronics.^[1–5] Methods of CNT production involving the catalytic decomposition of hydrocarbons in the presence of metal, as a by-product of arc-discharge or hydrocarbon flame production of fullerenes, laser vaporization, plasma-enhanced and thermal chemical vapor deposition, are well-established.^[6–11] The initial conception of CNTs as being perfectly seamless cylindrical structures of graphene layers without defects (except at the caps), has been shown to be oversimplified from experimental evidence.^[12] Zhou and coworkers performed intercalation/deintercalation of potassium and rubidium on compressed CNTs to show that the samples formed paper-mache structures of small groups of graphite sheets instead of crystalline CNTs (c-CNTs).^[13] Also, using electron

nano-diffraction techniques, Liu and Cowley showed that both helical and non-helical CNTs exist, and the tube cross-section could be either circular or polygonal.^[14] Amorphous CNTs (a-CNT) are carbon nanotubes that have non-hexagonal carbon rings (topological disorder), and cannot be represented by the proposed Russian doll model for CNTs.^[15,16] In recent years, a-CNTs have received increased attention due to their ease of growth^[17–19] and their applications in areas like field-emission display devices, gaseous adsorbents, energy storage, and catalyst support materials.^[20–22] Evidently, the development of these a-CNT-based devices requires a good understanding of their atomistic properties. This fact, coupled with the cost and technical difficulties associated with nano-scale experimental analysis, emphasizes the need to employ simulations as a tool for a preliminary and fundamental understanding of the atomistic structure and properties of a-CNTs.

An underlying motive for this work is discovering synthetic forms of graphite from available carbonaceous materials like coal. Within significant density and temperature windows, carbon allotropes have a remarkable proclivity to form layers, whether as graphene layers in graphite, spherical shells in “buckyballs” fullerenes, or cylindrical tubes in CNTs. In earlier works, we predicted the formation of amorphous graphite, which consist of layers of graphene with 5- and 7- member rings in the hexagonal network,^[23] and multi-shell fullerenes with topological defects.^[24] Theoretical studies of c-CNT are available,^[4] but this is


1. Introduction

Owing to their unique structure, mechanical strength, variable electrical properties, and high thermal conductivity, carbon

C. Ugwumadu, D. A. Drabold
Department of Physics and Astronomy
Nanoscale and Quantum Phenomena Institute (NQPI)
Ohio University
Athens, OH 45701, USA
E-mail: cu884120@ohio.edu; drabold@ohio.edu

R. Thapa
Institute for Functional Materials and Devices
Lehigh University
Bethlehem, PA 18015, USA

Y. Al-Majali, J. Trembly
Russ College of Engineering and Technology
Ohio University
Athens, Ohio 45701, USA

 The ORCID identification number(s) for the author(s) of this article can be found under <https://doi.org/10.1002/pssb.202200527>.

© 2022 The Authors. physica status solidi (b) basic solid state physics published by Wiley-VCH GmbH. This is an open access article under the terms of the Creative Commons Attribution License, which permits use, distribution and reproduction in any medium, provided the original work is properly cited.

DOI: 10.1002/pssb.202200527

not the case for a-CNTs. Hence, in this work, we explore the atomistic formation and properties of capped and hollow structures of single-wall a-CNT (a-SWCNT) and multi-walled a-CNT (a-MWCNT) obtained from initially random configurations of carbon atoms. The models were simulated using the accurate density-functional-theory (DFT) trained machine-learning Gaussian Approximation Potential (GAP)^[25] as implemented in the “Large-scale Atomic/Molecular Massively Parallel Simulator” (LAMMPS) software package.^[26] We emphasize that one importance of this work is the formation of ordered carbon structures from disordered structural configurations. The a-CNT models formed were validated using ab initio molecular dynamics (AIMD) packages including the plane-wave basis set DFT code, VASP (Vienna Ab initio Simulation Package),^[27] and the atomic orbital-based package, SIESTA (Spanish Initiative for Electronic Simulations with Thousands of Atoms).^[28] The electronic structure and transport, as well as the origin of inter-wall cohesion in a-CNTs, are discussed in detail. We explore the vibration signatures in a-CNT by computing the density of states and their corresponding inverse participation ratio, phase quotient, and bond stretching character. Finally, we provide an estimate for the average thermal conductivity in a-CNT. We also provide animations from our work and described them in Section S1, Supporting Information. For where it applies, two exchange-correlation functionals were used for the DFT calculations within VASP. These are the generalized gradient approximation (GGA) of Perdew–Burke–Ernzerhof (referred to as PBE)^[29] and the combination of the Slater exchange^[30] with the Perdew–Zunger parametrization of Ceperley–Alder Monte–Carlo correlation data in the local density approximation^[31,32] (referred to as LDA). However, except where explicitly stated, the results discussed herein are those obtained using the PBE functional.

2. Computational Method

The carbon nanotube generator applet, developed by Veiga and co-workers,^[33] was used in constructing a 400 atom, armchair crystalline CNT model ($n, m = 10$) that is discussed in this work. For the amorphous CNT models, we utilized the GAP C–C interatomic potential, which was trained on an extended set of reference data that was obtained from DFT-LDA simulations.^[25,34–37] The starting models were arranged as cylindrical bulks of randomly positioned carbon atoms that are at least 1.43 Å apart. The symmetry in the geometry of CNTs required that the models were formed by including the periodic boundary condition (PBC) in one dimension, call it the z -axis, while the capped a-CNTs were formed by adding a narrow space of 3.5 Å in the z -axis between the cylinders. Without PBC in the x - and y -directions, the magnitude of the input variables (like the density, diameter, height ...) required to successfully simulate a-CNT becomes non-trivial. To obtain good a-CNT models as shown in **Figure 1**, we trained a Random Forest (RF) classifier^[38–40] on a set of forming/non-forming models (refer to **Figure 2**) to predict the important input variables (features), and a decision tree model to obtain their acceptable range of values. RF is a parallel ensemble learning technique that combines multiple decision tree algorithms^[41] and involves a voting process that exploits those algorithms to

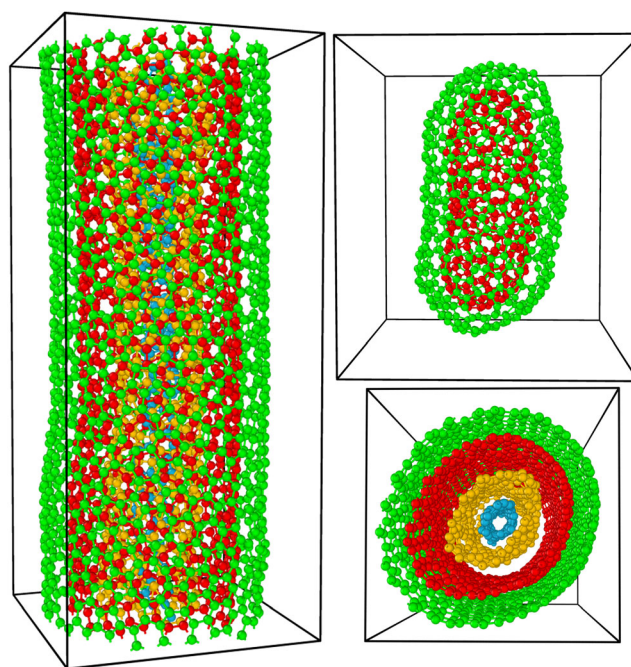


Figure 1. Figure showing some a-CNT models with 3-fold coordination for each atom. The colors indicate the number of tubes in the a-MWCNT.

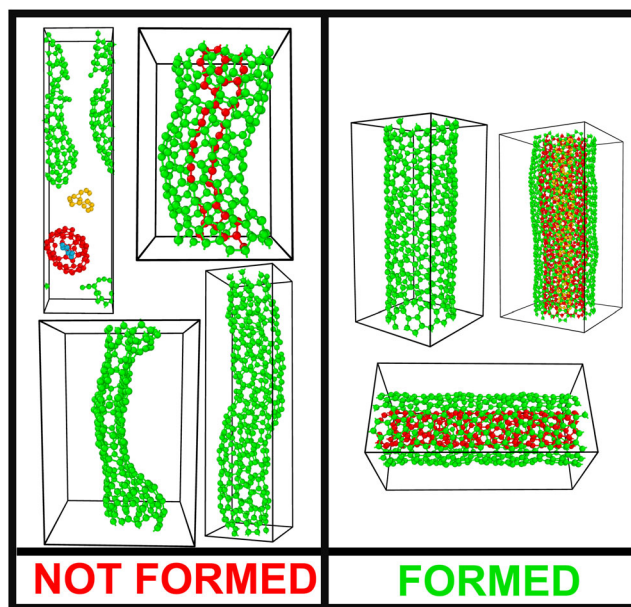


Figure 2. Examples of models that do not form [LEFT] and models that form [RIGHT] a-CNT based on their input variables.

obtain a better predictive performance. It uses random sampling of the training data set (with replacement) in building decision trees and for splitting the nodes in the network. In the RF implementation, the height (H) and diameter (d) of the models were substituted by a unit-less parameter (aspect ratio; $AR = H/d$). At the initial stage, the parameters used in building the training dataset were sampled uniformly within reasonable limits

(AR: 1–12; system size: 200–1500 atoms (in multiples of 40); vacuum in the x - y plane: 1–10 Å; cutoff radius: 1.4–1.7 Å), which ensured that the initial configuration was constrained to form a cylindrical shape. The final configurations obtained after MD simulations were labeled as “formed” (label = 1) or “not-formed” (label = 0) a-CNT. In addition to human validation, we automated the labeling process by using an “in-house” Model Filtering and Scoring Algorithm (MoFaSA) that assigns labels to models from a scoring metric. The scoring metric estimates the shape of the model, based on a combination of clustering analysis (to identify non-connecting nanotube walls) and shape descriptors (like asphericity, acylindricity, and relative shape anisotropy). These shape characterizations are implemented on a surface reconstruction of the atomic coordinates of each cluster using the alpha-shape method^[42] on a constructed Delaunay tessellation.^[43,44] An illustration of the decisions made by MoFaSA on different configurations is presented in Figure 2. With a total of 850 labeled models, the next step involved using RF in ranking the features by their level of importance, aimed at reducing the number of variables required in generating additional training dataset. The feature importance is an implicit selection process implemented in RF that can be obtained using the Gini impurity criterion given as^[45]

$$G(t) = 1 - \sum_{i=1}^m P(i|t)^2 \quad (1)$$

The summation is over all the classes (t) in a training set (m), and $P(i|t)$ is the probability that a randomly selected training example (i) is correctly classified. The Gini scores for ranking the parameters (feature importance) for a K -fold ($K = 4$) cross-validation set are shown in Table 1 and plotted as a radar chart in Figure S1, Supporting Information. The prediction revealed that the aspect ratio and system size are the most important features. While the average energy is obtained at the end of the simulation, it serves as an important feature during training since well-formed a-CNTs have lower total energies compared to the deformed structures. Also, as our ML model is applied post-MD, it is still reasonable to use the energy as a feature. Next, we trained a decision tree classifier to obtain a decision boundary that infers a range of suitable AR for the initial configuration (see a representative decision tree in Figure S2, Supporting

Table 1. Table showing the important feature index predicted from a random forest classifier with $K = 4$ cross-validation set. It also shows the accuracy rate on the test set for each fold and the mean and standard deviation calculated for scaling the aspect ratio and system size for the decision boundary construction. See discussion in the Supporting Information.

| | Kfold-1 | Kfold-2 | Kfold-3 | Kfold-4 | Mean | Std |
|-----------------------------------|---------|---------|---------|---------|------|------|
| Aspect ratio (height/diameter) | 0.32 | 0.34 | 0.32 | 0.33 | 4.3 | 1.25 |
| System size (no. of atoms) | 0.18 | 0.20 | 0.19 | 0.23 | 1672 | 883 |
| Cutoff radius [Å] | 0.13 | 0.12 | 0.12 | 0.08 | | |
| Vacuum in the x - y plane [Å] | 0.11 | 0.12 | 0.12 | 0.13 | | |
| Energy [eV atom ⁻¹] | 0.25 | 0.22 | 0.25 | 0.23 | | |
| Accuracy [%] | 87 | 92 | 87 | 89 | | |

Information). We generated 634 new training models with a different set of parameter distributions, based on the predictions obtained from the initial dataset. The cutoff radius was fixed at 1.43 Å. The amount of vacuum in the x - y plane and the system size was uniformly sampled between 3–6 Å and 200–3200 atoms (in increments of 20) respectively, and AR was sampled in a normal distribution with a mean value of 4.3 and standard deviation of 1.2. An instance of the decision boundary is shown in Figure 3. The orange region in the plot indicates that the optimal AR range is between 0.32–0.51. The black and grey scatter points are predictions made by our ML model on a test set for a range of input variables that formed (value = 1) or did not form (value = 0) a-CNT respectively. It shows that the decision boundary from our classifier makes a close to accurate prediction on unseen data. Before implementing the decision tree algorithm, the features were scaled by subtracting the mean of the distribution and by dividing the result by the standard deviation. The mean and standard deviation used for AR and system size are shown in Table 1.

For all a-CNT models in this work, the MD simulation protocol involved sampling the atomic positions and velocities on the canonical ensemble using a Nosé-Hoover thermostat at a fixed temperature of 3000 K for 240 ps with a timestep of 1 fs. Next, the models were allowed to find a more energetically and structurally favorable configuration by cooling to room temperature at a rate of $2.7 \times 10^{13} \text{ K s}^{-1}$. We stress that the cooling rate does not alter bonds formed during or after heating. Finally, the structures were relaxed using the conjugate gradient (CG) algorithm as implemented within LAMMPS with a force tolerance of $10^{-6} \text{ eV Å}^{-1}$. We further validated the energies and structure of the final models by implementing DFT CG relaxation within VASP (using PBE and LDA functionals) and SIESTA. The energy difference between the GAP models and DFT-relaxed models ranged between $0.03 \text{ eV atom}^{-1} \leq \delta E \leq 0.07 \text{ eV atom}^{-1}$, and the relaxation process did not lead to bond breaking or forming. This confirmed that the atoms are formed in energetically stable

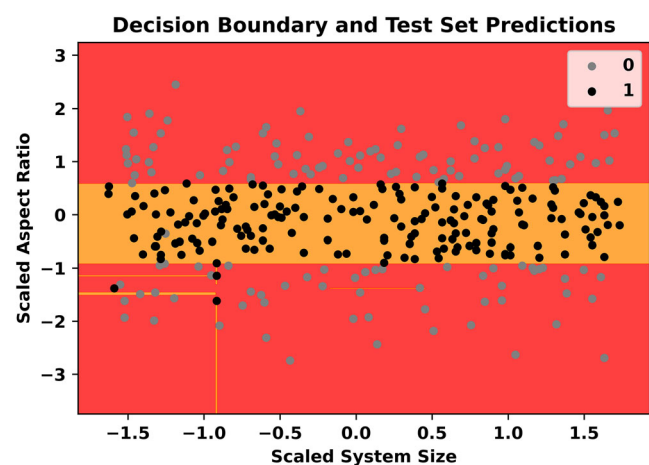


Figure 3. The decision boundary from a decision tree model using the aspect ratio and system size as features. 1 means an acceptable a-CNT formed, while 0 indicates otherwise. The feature values were scaled by subtracting the mean of the distribution and dividing the result by the standard deviation. The mean and standard deviation used for AR and system size are shown in Table 1.

and realistic local configurations. The size of the models generated ranges from 200 atoms to 3200 atoms, forming both a-SWCNT and a-MWCNTs (up to 4 walls). The models will henceforth be referred to as a-CNT_N, where *N* is the number of atoms. In the discussions that follow, we have selected 10 independent models with *N* = 200 (a-SWCNT), 400, 840, and 2000 (a-MWCNT) atoms (40 models in total).

3. Results and Discussion

3.1. Formation and Nano-Structure

We have provided animations showing the time evolution in the formation of capped and hollow a-CNT in the Supporting Information. The a-CNTs were observed to form an outermost tube first, which is followed by the formation of the inner tube(s). This formation process is similar to what we observed in a different work with multi-shell, non-classical fullerenes.^[24] The final models have diameters ranging from 0.5 to 2 nm for a-CNT with up to 4 walls, and the average gallery (space between any 2 consecutive layers) in the a-MWCNTs models was calculated to be 0.31 nm, which is within the range that had been reported in experiments^[46] and also close to the inter-layer spacing in graphite. The structural order of the a-CNT models was analyzed from the radial distribution function (RDF). In **Figure 4**, the peaks obtained for the a-CNT models were compared with those from the generated armchair c-CNT model and amorphous Carbon (a-Carbon)^[47] model. The RDF peak for the first shell in all the a-CNT models was close to the C–C bond length observed in c-CNT and graphite. Notably, the RDF of a-CNT₂₀₀, which is a single-walled a-CNT, has similar features resembling a-carbon and only the multi-walled a-CNT models reproduced the third c-CNT peak around 2.84 Å. This is a consequence of the higher ratio of hexagonal to non-hexagonal rings (6:*n*; *n* = 5 or 7) observed in a-CNTs which have larger system sizes. The size of the topological defects, which are the non-hexagonal arrangements of carbon atoms incorporated in the hexagonal network, was calculated using King's criterion

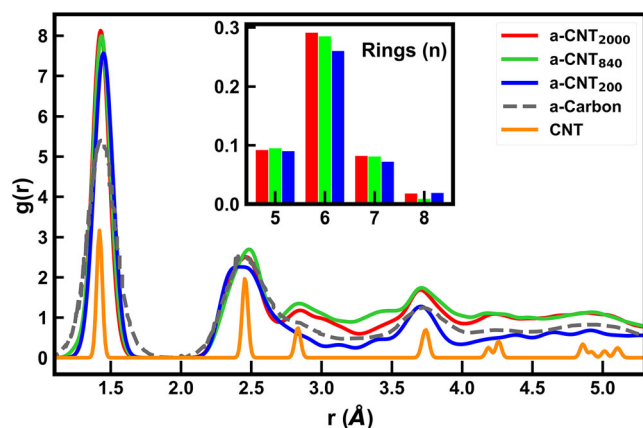


Figure 4. Radial distribution function $g(r)$ for different a-CNT models compared with crystalline CNT (c-CNT) and amorphous Carbon (a-Carbon). The inset shows the ring distribution obtained using King's criterion for ring statistics.

for ring statistics^[48] (see inset in **Figure 4**) and it showed similar values for all the a-MWCNTs with a slight decrease observed for a-SWCNTs.

Defects in nanostructures like CNT play a role in their morphology and chemical properties. Experimentally and otherwise, an accurate and quantitative description of the defects or a standard for distinguishing them is still needed. To this end, we studied the ring defects in the a-CNT models, **Figure 5a–f** shows all the possible defects that exist in the a-CNT models. **Figure 5a–c** are the Stone-Wales (SW; 5665), 5675, and Stone-Thrower-Wales (STW; 5775) defects respectively. We refer to these defects (a–c) as primary defects because they can exist alone in the hexagonal C network. On the other hand, **Figure 5d–f** are the inverse Stone-Thrower-Wales (ISTW; 7557 + 57), 7558 + 57, and 7557 + 7558 defects respectively. They are termed secondary defects because they are combinations of two distinct defects. In **Figure 5**, the blue ellipses that are positioned over the C atoms that connects 2 pentagonal rings in the defect sites, are used to classify the defect type. It engulfs two connecting vertex atoms in **Figure 5a–c** and two shared basal atoms in **Figure 5d–f**. The 57, STW, and ISTW defects are well-known defects in carbon nanotubes,^[49–54] but to our knowledge, there is no report on the 5675 and 7558 defects; hence, this is the first time such defects will be reported for any layered carbon network. We note that the heptagon-pentagon and octagon-pentagon ring connections still preserve the 3-fold coordination of the C atoms.

3.2. Electronic Structure, Transport, and π -Electron Delocalization

The electronic density of states (EDoS) for a-CNT was computed within VASP and the extent of localization of Kohn-Sham states (ϕ) was calculated as the electronic inverse participation ratio (EIPR) using the following equation

$$I(\phi_n) = \frac{\sum_i |a_n^i|^4}{(\sum_i |a_n^i|^2)^2} \quad (2)$$

where a_n^i is the contribution to the eigenvector (ϕ_n) from the *i*th atomic orbital. High (low) values of EIPR indicate localized (extended) states. The Fermi-level (E_f) in the EDoS and EIPR plots in **Figure 6** was shifted to zero. The EDoS plots for a-CNT do not show any spectral gap at E_f , and a few electronic states appear localized around the Fermi level. The non-zero gap (NZG) observed for a-CNTs has been reported for armchair SWCNTs, as well as SWCNTs with $n - m \neq 3\zeta$, where ζ is a positive integer.^[55,56] In addition to the NZG similarity in armchair c-CNT and a-CNT EDoS, we found that replicated periodic images of both structures in the *z*-direction share a degree of structural similarity as well (see left (right) inset in **Figure 6** for a-CNT (c-CNT)). The effect of disorder in the a-CNTs network on the electronic conduction active path was analyzed by projecting the electronic conductivity into a spatial grid. This involved an implementation of the space-projected conductivity (SPC) formalism which exploits the Kubo–Greenwood formula (KGF) to obtain information about the conduction pathways in materials.^[57,58] **Figure 7** is a representation of the conduction path observed in a-CNT. We found that a-CNT favored axially directed

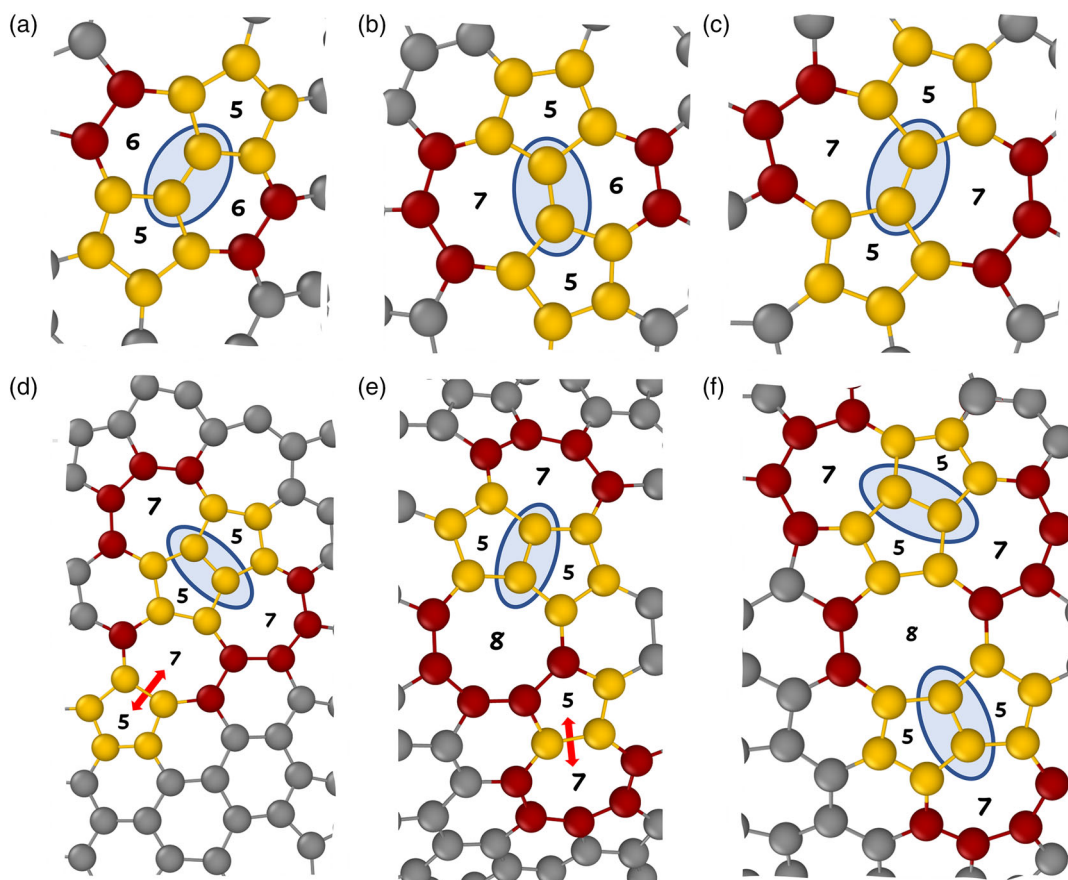


Figure 5. Figure showing primary ring defects in a-CNT. These defects are a) Stone-Wales (5665), b) 5675, and c) Stone-Thrower-Wales (5775) defects, which are the primary defects. The secondary ring defects in a-CNT are the d) inverse Stone-Thrower-Wales (7557) + 57, e) 7558 + 57, f) 7557 + 7558 defects. The blue ring indicates the connecting vertex atoms (a–c) or shared basal atoms (d–f) in pentagon-forming rings, from which we classify the defects.

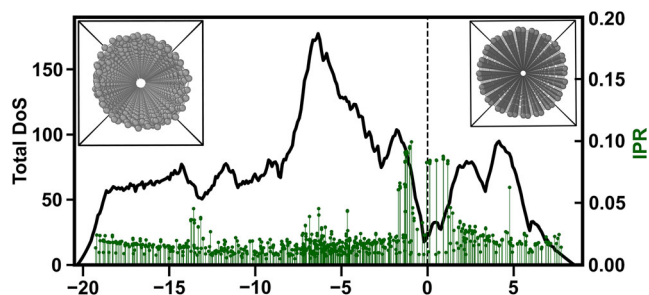


Figure 6. Electronic density of states for a-CNT. The [LEFT] and [RIGHT] insets compare the structure of a-CNT and armchair CNT. The periodic images of the models were replicated in the z-direction.

conduction paths along connected hexagonal carbon rings. This axial electronic conduction path is consistent with published results for crystalline carbon nanotubes.^[59–61] While the presence of non-hexagonal rings in a-CNT restricts electron flow in the network, this effect is not as pronounced as it is in amorphous graphite.^[23] As shown in Figure 7, the 7-member ring does not completely terminate the conduction path but rather

acts as a bifurcation of the electron transport initially in the path along the yellow-colored C atoms into the path indicated by the red-colored C atoms. On the other hand, SPC analysis on the generated c-CNT model showed ballistic electronic transport i.e., without scattering (see Figure S3, Supporting Information), which has been confirmed in experiments,^[59,62] as well as by theoretical calculations.^[63] The deviation from ballistic conductivity in a-CNT supports the premise that topological defects influence electronic properties and transport in carbon nanotubes.^[64–67] The conduction path in a-CNT is unique, as it differs from one model to another because of the randomness of the topological defects. This property thus provides potential technological applications for a-CNTs as base materials in electronic devices that require unique paths for electronic transport. An example is the Physical Unclonable Functions (PUFs), which are state-of-the-art secret key generators for advanced security, especially in the Internet of Things (IoT). Moon and co-workers achieved an implementation of c-CNT-based PUFs by placing a network of all-printed single-wall c-CNTs between multiple electrodes, thereby increasing the variation in the distribution and range of the resistance within and across the c-CNT network.^[68] In the amorphous regime, amorphous sub-stoichiometric silicon

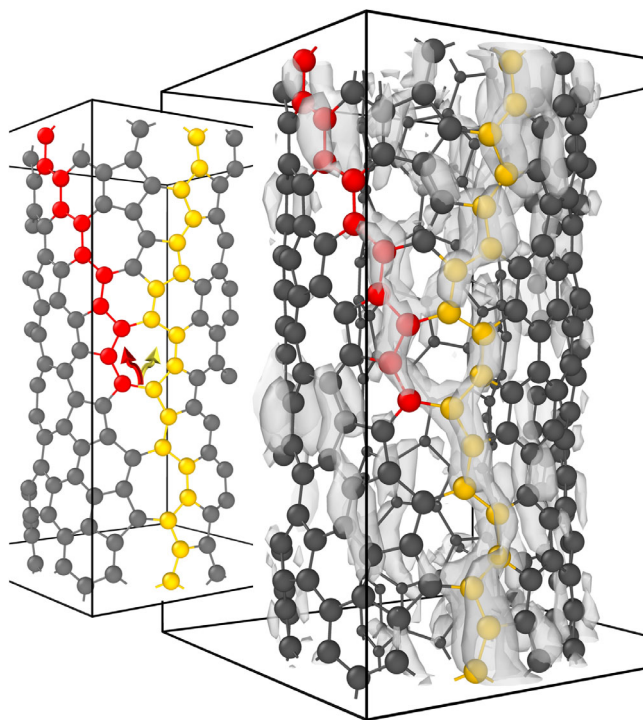


Figure 7. Spatially projected electronic conductivity in a-CNT. The presence of the 7-member ring defect causes a bifurcation of the electronic conduction path on the yellow-colored C atom into the red-colored atom. The conductivity path is the white transparent blob.

oxides, like $\text{SiO}_{1.3}$, have been confirmed to be promising base materials for PUF device fabrication,^[69] owing to their unique electronic conduction path that is inherent from topological defects induced by the oxygen vacancy sites.^[70] Similarly, the random distribution of the topological defects in a-CNT also provides it with a unique conduction path that varies from one model to another, which can make it a viable base material

for PUF device fabrication as well. Additionally, Behinia and Rahimi showed that engineering topological defects into c-CNTs allows for specific electronic conduction paths, which is useful in the design of nanoscale electrical switches.^[71] Qualitative calculation of the average KGF conductivity for the models revealed that the conductivity of a-CNT decreased by a factor of order 10^2 when compared to the crystalline CNT, and this is in agreement with the experimental reports in refs. [60,72].

Inter-layer cohesion in layered carbon structures derives from a combination of Van der Waals forces and delocalized electrons originating from occupied states near the Fermi level ($E < E_f$).^[23] These states are linear combinations of π -orbitals that are projected in the normal direction to the local plane defined by each sp^2 carbon atom. For the a-CNT models, the contribution of the electrons in the π subspace was decomposed from the total electronic charge density and projected as isosurfaces on sliced partitions. **Figure 8** shows the π -electron distribution for ten bands closest to the Fermi level. Figure 8a shows the π -electron distribution on a single slice of a 400 atom a-CNT model. The atoms contributing to that particular slice are shown in Figure 8b. The red atoms (R1) are above the green plane, which is the slice being considered. There are 2 shades of black in Figure 8b, the lighter (B1) and darker (B2) shades of black correspond to atoms that are below and intersect the green plane respectively. The reader can find a 3D visualization of contributing atoms in Figure S4, Supporting Information, which is a CW rotation of Figure 8b. In Figure 8c, the π -electron density is normalized to the maximum value in the slice and mapped to a mesh grid with zero values (colored as black) to increase the contrast in the π -electron density distribution. We have labeled the atom positions in Figure 8a that corresponds to Figure 8b. In Figure 8a, o , x and x^* and corresponds to R1, B1 and B2 atoms respectively. x^- and o^- are atoms within the region that do not contribute to the π orbital. xo indicates a combined contribution of two atoms (x and o) to the charge density. The figure shows a slice that was taken at 1.9 \AA from the origin and Figure S5,

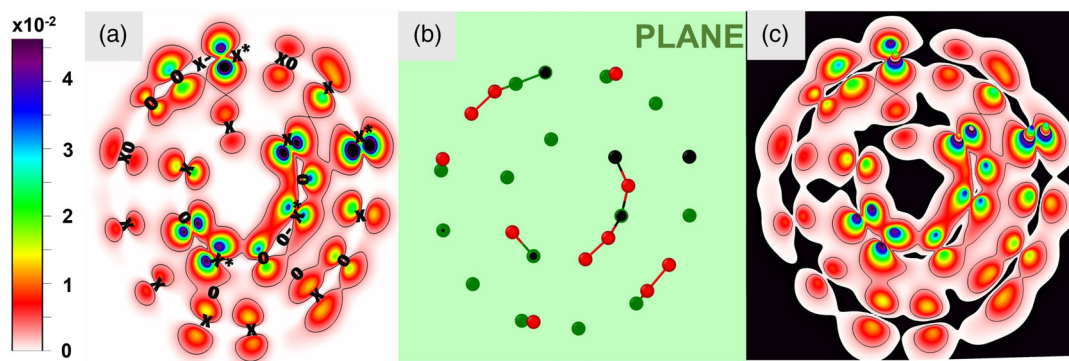


Figure 8. The figure in (a) shows the π -electron distribution on a single slice of a 400 atom a-CNT model. The atoms contributing to that particular slice are shown in (b). In (b), the red atoms (R1) are above the green plane (the slice being considered). There are 2 shades of black in (b), the light (B1) and dark (B2) shades correspond to atoms that are below and intersect the green plane respectively. In the plot in (c), the π -electron density is normalized to the maximum value in the slice and mapped to a mesh grid with zero values (colored as black) to increase the contrast in the π -electron density distribution. We have labeled the atoms positions in (a) that corresponds to (b). In (a) x and o correspond to B1 and R1 atoms, respectively. x^* are B2 atoms. x^- and o^- are atoms within the region that do not contribute to the π orbital, while xo indicate a combined contribution of two atoms (x and o). The figure shows a slice was taken at 1.9 \AA from the origin. An animation, PiBandDensity_mov.mp4 in the Supporting Information shows variations in the π -electron distribution for multiple slices across the a-CNT₄₀₀ model discussed here.

Supporting Information shows the slicing pattern implemented on the a-CNT₄₀₀ model. The choice of 1.9 Å is arbitrary and we have provided an animation (PiBandDensity_mov.mp4) in the Supporting Information that shows variations in the π -electron distribution for multiple slices across the a-CNT₄₀₀ model discussed here. The cross-interaction of the quasi-free π -electrons in the gallery poses weak metallic bonding between the tubes,^[73] and this contributes to the cohesion between the layers.^[23,24,74,75]

In a-CNT, the maximum value for the π -electron density is $\approx 10\%$ of the maximum total charge distribution in all the bands, and it is also $\approx 2.75\%$ of the maximum total charge distribution around the center of the gallery. We show here that dispersive forces beyond the local density approximation are not necessary to form inter-wall tubes, and such corrections have little effect on the final tube geometries. In our simulation of amorphous graphite,^[23] the inclusion of Van der Waals corrections in the VASP implementation^[76] did not show any appreciable difference in the total energy when compared to that of the GAP models. The values observed at the center of the gallery in a-CNTs were lower than those from amorphous multi-shell fullerenes ($\approx 4.3\%$)^[24] but larger than amorphous graphite ($\approx 2.0\%$).^[23] The mid-gallery values for these amorphous carbon allotropes are influenced by the local atomic curvature and by the degree of the linear combination (cross-interaction) of the Kohn-Sham orbitals describing the π -bands. It is noteworthy that in the amorphous phase of these layered carbon structures, layering persists despite the absence of an exact graphite stacking registry.

3.3. Vibrations and Thermal Conductivity

Carbon nanotube samples that are produced in the laboratory are not always perfect crystals and may include non-hexagonal carbon rings. Additionally, there could be impurities (like fullerenes, graphitic and amorphous carbon, carbon nanoparticles, etc.) in the samples^[49] and this can lead to confusion in the interpretation of experimental vibrational spectra. In **Figure 9** we present a vibrational spectrum that may be an experimentally comparable fingerprint of a-CNT from methods like Raman^[77–79] and infra-red^[80–82] spectroscopy. The atomic vibrational density of states was calculated within the harmonic approximation model as

$$g(\omega) = \frac{1}{3N} \sum_{i=1}^{3N} \delta(\omega - \omega_i) \quad (3)$$

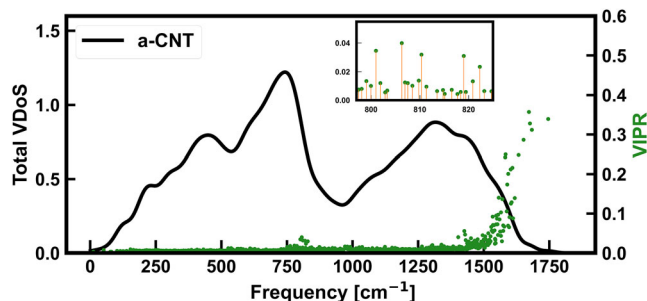


Figure 9. Figure showing the total VDoS and VIPR for a-CNT calculated from the harmonic approximation. The inset shows the VIPR around 797, 825 cm^{-1} .

where, N and ω_i represent the number of atoms and the eigen-frequencies of normal modes, respectively. The δ function (approximated by a Gaussian with a standard deviation equal to 1.5% of the maximum frequency) was employed. The (green) scatter plot in **Figure 9** is the vibrational inverse participation ratio (VIPR) that indicates the extent of localization of each normal mode frequency.^[24] Low values of VIPR indicate vibrational modes that are distributed among a large number of atoms while higher values imply that few atoms contribute at that particular eigen-frequency. Additionally, the region where $\text{VIPR} \gtrsim 0.15$ is considered the transition frequency from diffusons to locons^[83] and is found to be at around 1582 cm^{-1} in a-CNT. The lack of periodicity in the a-CNT lattice restricts vibrations to non-propagating modes (e.g., diffusons and locons).^[84,85] This means that, unlike crystals, vibrational modes in amorphous systems cannot be rigorously classified into purely acoustic (at low-frequency spectrum) and purely optical (at high-frequency spectrum). However, the phase quotient (Q_p) of Bell and Hibbins–Butler^[86] provides a statistical measure for classifying the modes as in-phase (acoustic mode) and out-of-phase (optical mode) with respect to neighbouring atoms. The normalized Q_p is given as^[85]

$$Q_p = \frac{1}{N_b} \frac{\sum_m u_n^i \cdot u_n^j}{\sum_m |u_n^i \cdot u_n^j|} \quad (4)$$

where N_b is the number of valance bonds, u_n^i and u_n^j are the normalized displacement vectors for the n th normal mode. The index, i , summed over all atoms and j enumerates neighboring atoms of the i th atom. The in-phase vibration of the bulk material gives $Q_p = 1$ (purely acoustic). Conversely, a value of -1 would correspond to motion in the opposite direction between neighboring atoms (purely optical). It then follows that positive (negative) Q_p is more “acoustic-like” (“optical-like”). Another important tool for understanding vibrations is the bond-bending or bond-stretching character ($S(\omega)$) given as

$$S(\omega_n) = \frac{\sum_m |u_n^i - u_n^j| \cdot \hat{r}_{ij}}{\sum_m |u_n^i - u_n^j|} \quad (5)$$

where, u_n^i is as in Equation (4) and \hat{r}_{ij} is the unit vector parallel to the m th bond. $S(\omega_n)$ is close to unity when the mode of vibration is predominantly of bond-stretching type and will be close to 0 otherwise. **Figure 10** shows Q_p [TOP] and $S(\omega_n)$ [BOTTOM] for a double-walled a-CNT (DWCNT) with 400 atoms. We have provided animations to visualize the vibrations in the Supporting Information. The mid-frequency region around $800\text{--}820 \text{ cm}^{-1}$ shows some localization (see inset in **Figure 9**) and a local minimum at $\approx 807 \text{ cm}^{-1}$, which is also ≈ 0 in the for Q_p plot. The behavior of Q_p around 0 cannot be interpreted as acoustic- or optical-like modes. The animation, freq_807.mp4, shows that the modes in this region are quasi-localized resonant modes^[87] since they are distributed over a number of atoms and also are not diffuson to locon transition frequencies. Other notable vibrations in the double-wall a-CNT analyzed are at 32, 44, 55 cm^{-1} , which correspond to twisting vibrations of the outer shell, translation, and twisting vibration of the inner shell respectively (see Supporting Information for animations of these

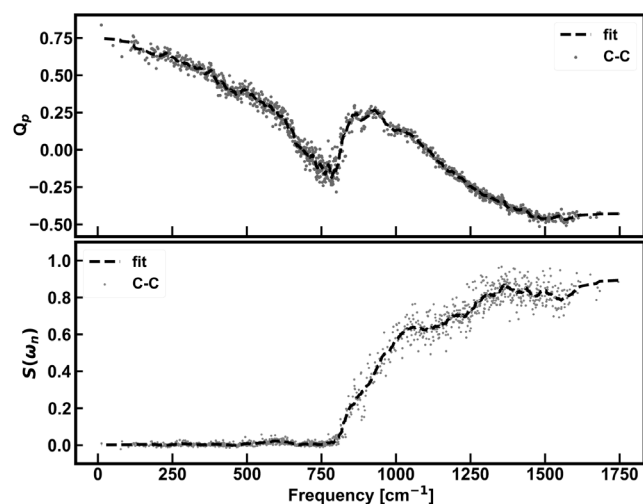


Figure 10. Figure showing the [TOP] phase quotient and [BOTTOM] stretching character of a-CNT.

modes). We emphasize that the twisting modes of a particular tube at a given frequency cost very little energy. This is because the electron gas in the gallery between layers is quite diffuse and it is weakly correlated with particular atoms in the layer, so the energy dependence of the system, to the first approximation, is on the distance between the shells and not affected by the angle. The radial breathing modes (RBMs) which dominate the low-frequency Raman spectrum in experiments are unique to specific MWCNTs and much focus has been given to the research of RBM because of its importance in the applications of structure and property characterizations.^[88–90] We observed an in-phase, low-frequency RBM at around 81 cm^{-1} (see animation in Supporting Information). RBM in MWCNTs has been observed experimentally from Raman-active peaks around 100 cm^{-1} ,^[89] and in-phase RBM at around $94\text{ (}85\text{) cm}^{-1}$ have been predicted for armchair DWCNT (SWCNT).^[91] We note here that the similarities observed between a-CNT and the armchair CNT could be a path worth exploring.

Finally, we describe the effect of topological defects on the thermal conductivity (TC) of a-CNTs. Heat conduction in carbon materials is usually dominated by phonons (even in graphite);^[92] this allows us to consider the contribution of the heat flux (J) for each atom^[93,94] in a 2000 atom a-MWCNT and then relate an ensemble average of the auto-correlation of J to the TC (κ) using the Green–Kubo formula given as^[95,96]

$$\kappa = \frac{1}{3Vk_B T^2} \int_0^\tau \langle J(0) \cdot J(t) \rangle dt \quad (6)$$

where V , T , and k_B are the system volume, temperature, and Boltzmann's constant, respectively. The upper limit of the integral was approximated by τ ($= 2\text{ ns}$), which is the correlation time required for the heat current auto-correlation to decay to zero. The TC was obtained by averaging the integral in Equation (6) from 10 independent models. The Nosé–Hoover thermostat^[97,98] was used for thermalization and equilibration at $T = 300\text{ K}$ at a fixed volume using a 1 fs time-step, and at the beginning of the

simulation, initial velocities were assigned to the atoms randomly from a Gaussian distribution. Our result showed that the average TC calculated for a-CNT was $22.15\text{ Wm}^{-1}\text{ K}^{-1}$ at 300 K . The thermal conductivity of MWCNT is $\approx 3000\text{ Wm}^{-1}\text{ K}^{-1}$,^[99,100] so the thermal conductivity of a-MWCNT is an order of 10^2 less than c-MWCNT, which is similar to what we have reported for the electrical conductivity, respecting a sort of Wiedemann–Franz rule^[101] for nanotubes.

4. Conclusion

In this work, we explored the formation of a-CNT starting from an initially random configuration of carbon atoms using the GAP potential. The starting configuration required eliminating the periodic boundary conditions in the x – y plane only. The complexity involved in the choice of the important variables to simulate realistic a-CNTs was minimized by learning the important features from a random forest implementation. The structure of the a-CNT models was validated by conjugate gradient relaxation as implemented within SIESTA and VASP. The diameter of the a-CNTs ranged from 0.5 nm in a-SWCNTs to 2 nm in a-MWCNTs, and the inter-wall spacing was $\approx 0.31\text{ nm}$. The ring defects in a-CNTs were discussed and a potentially new type of defect was observed. Electronic structure analysis showed that there was no band-gap at the Fermi level, which is a property observed in all armchair CNTs. The delocalized π -electrons in the gallery were confirmed to be involved in the inter-layer cohesion in a-CNTs. The density of states and corresponding participation ratio for the phonon vibrations were analyzed, and the result showed that a-CNTs have localized states only at the high-frequency end of the vibration spectrum which is consistent with other amorphous structures. The phase quotient and stretching character analysis further suggested that those localized sites were from atoms participating in non-hexagonal rings. The average thermal conductivity for a-CNT was $22.15\text{ Wcm}^{-1}\text{ K}^{-1}$ at room temperature and is an order of 10^2 less than crystalline MWCNT, which was also similar to the average thermal conductivity. In conclusion, the strong proclivity to form layered structures from chaotic configuration, even with topological defects, remains one of the wonders of carbon.

Supporting Information

Supporting Information is available from the Wiley Online Library or from the author.

Acknowledgements

We thank Ms. Anna-Theresa Kirchttag for proofreading the manuscript. We also thank the U.S. Department of Energy for support under Grant No. DE-FE0031981 and XSEDE (supported by National Science Foundation Grant No. ACI-1548562) for computational support under allocation no. DMR-190008P.

Conflict of Interest

The authors declare no conflict of interest.

Data Availability Statement

The data that support the findings of this study are available in the supplementary material of this article.

Keywords

amorphous solids, carbon, Gaussian Approximation Potential, nanotubes

Received: November 6, 2022

Revised: December 19, 2022

Published online:

- [1] N. Anzar, R. Hasan, M. Tyagi, N. Yadav, J. Narang, *Sens. Int.* **2020**, *1*, 100003.
- [2] N. M. Saifuddin, A. Z. Raziah, A. R. Junizah, *J. Chem.* **2013**, *2013*, 676815.
- [3] M. Shokrieh, R. Rafiee, *Mech. Compos. Mater.* **2010**, *46*, 155.
- [4] R. Rafiee, R. M. Moghadam, *Composites, Part B: Eng.* **2014**, *56*, 435.
- [5] L. S. Salah, N. Ouslimani, D. Bousba, I. Huynen, Y. Danlée, H. Aksas, *J. Nanomater.* **2021**, *2021*, 4972770.
- [6] R. Baker, *Carbon* **1989**, *27*, 315.
- [7] A. Oberlin, M. Endo, T. Koyama, *J. Cryst. Growth* **1976**, *32*, 335.
- [8] A. M. Benito, Y. Maniette, E. Muñoz, M. Martinez, *Carbon* **1998**, *36*, 681.
- [9] S. Iijima, *Nature* **1991**, *354*, 56.
- [10] P. Mahanandia, P. Vishwakarma, K. Nanda, V. Prasad, S. Subramanyam, S. Dev, P. Satyam, *Mater. Res. Bull.* **2006**, *41*, 2311.
- [11] P. J. Harris, P. J. F. Harris, *Carbon Nanotube Science: Synthesis, Properties and Applications*, Cambridge University Press, Cambridge **2009**.
- [12] T. Ebbesen, T. Takada, *Carbon* **1995**, *33*, 973.
- [13] O. Zhou, R. M. Fleming, D. W. Murphy, C. H. Chen, R. C. Haddon, A. P. Ramirez, S. H. Glarum, *Science* **1994**, *263*, 1744.
- [14] M. Liu, J. M. Cowley, *Ultramicroscopy* **1994**, *53*, 333.
- [15] Y. Maniwa, R. Fujiwara, H. Kira, H. Tou, E. Nishibori, M. Takata, M. Sakata, A. Fujiwara, X. Zhao, S. Iijima, Y. Ando, *Phys. Rev. B* **2001**, *64*, 073105.
- [16] F. Boi, X. Zhang, J. Borowiec, D. Medranda, S. Wang, K. Yan, J. Zhang, J. Wen, *Diamond Relat. Mater.* **2018**, *85*, 80.
- [17] K. H. Tan, R. Ahmad, B. F. Leo, M. C. Yew, B. C. Ang, M. R. Johan, *Mater. Res. Bull.* **2012**, *47*, 1849.
- [18] N. Zhao, C. He, X. Du, C. Shi, J. Li, L. Cui, *Carbon* **2006**, *44*, 1859.
- [19] N. Zhao, P. Zhang, L. Yang, L. Fu, B. Wang, Y. Wu, *Mater. Lett.* **2009**, *63*, 1955.
- [20] S. A. Zikalala, M. B. Chabalala, N. N. Gumbi, N. J. Coville, B. B. Mamba, B. K. Mutuma, E. N. Nxumalo, *RSC Adv.* **2021**, *11*, 6748.
- [21] D. Banerjee, U. K. Ghorai, N. S. Das, B. Das, S. Thakur, K. K. Chattopadhyay, *ACS Omega* **2018**, *3*, 6311.
- [22] A. Jha, D. Banerjee, K. Chattopadhyay, *Carbon* **2011**, *49*, 1272.
- [23] R. Thapa, C. Ugwumadu, K. Nepal, J. Trembly, D. A. Drabold, *Phys. Rev. Lett.* **2022**, *128*, 236402.
- [24] C. Ugwumadu, K. Nepal, R. Thapa, Y. Lee, Y. Al Majali, J. Trembly, D. Drabold, *Carbon Trends* **2022**, *10*, 100239.
- [25] V. L. Deringer, G. Csányi, *Phys. Rev. B* **2017**, *95*, 094203.
- [26] A. P. Thompson, H. M. Aktulga, R. Berger, D. S. Bolintineanu, W. M. Brown, P. S. Crozier, P. J. in 't Veld, A. Kohlmeyer, S. G. Moore, T. D. Nguyen, R. Shan, M. J. Stevens, J. Tranchida, C. Trott, S. J. Plimpton, *Comput. Phys. Commun.* **2022**, *271*, 108171.
- [27] G. Kresse, J. Furthmüller, *Phys. Rev. B* **1996**, *54*, 11169.
- [28] J. M. Soler, E. Artacho, J. D. Gale, A. García, J. Junquera, P. Ordejón, D. Sánchez-Portal, *J. Phys.: Condens. Matter* **2002**, *14*, 2745.
- [29] J. P. Perdew, K. Burke, M. Ernzerhof, *Phys. Rev. Lett.* **1996**, *77*, 3865.
- [30] P. A. Dirac, in *Mathematical Proceedings of the Cambridge Philosophical Society*, Vol. 26, Cambridge University Press, Cambridge **1930**, pp. 376–385.
- [31] D. M. Ceperley, B. J. Alder, *Phys. Rev. Lett.* **1980**, *45*, 566.
- [32] J. P. Perdew, A. Zunger, *Phys. Rev. B* **1981**, *23*, 5048.
- [33] R. G. A. Veiga, D. Tomanek, N. Frederick, TubeASP: Carbon Nanotube Generation Applet, **2022**.
- [34] V. L. Deringer, A. P. Bartók, N. Bernstein, D. M. Wilkins, M. Ceriotti, G. Csányi, *Chem. Rev.* **2021**, *121*, 10073.
- [35] M. A. Caro, G. Csányi, T. Laurila, V. L. Deringer, *Phys. Rev. B* **2020**, *102*, 174201.
- [36] V. L. Deringer, M. A. Caro, R. Jana, A. Aarva, S. R. Elliott, T. Laurila, G. Csányi, L. Pastewka, *Chem. Mater.* **2018**, *30*, 7438.
- [37] S. Fujikake, V. L. Deringer, T. H. Lee, M. Krynski, S. R. Elliott, G. Csányi, *J. Chem. Phys.* **2018**, *148*, 241714.
- [38] T. K. Ho, in *Proc. of 3rd Int. Conf. on Document Analysis and Recognition*, vol. 1, IEEE, Piscataway, NJ **1995**, pp. 278–282.
- [39] L. Breiman, *Mach. Learn.* **2001**, *45*, 5.
- [40] F. Pedregosa, G. Varoquaux, A. Gramfort, V. Michel, B. Thirion, O. Grisel, M. Blondel, P. Prettenhofer, R. Weiss, V. Dubourg, J. Vanderplas, A. Passos, D. Cournapeau, M. Brucher, M. Perrot, E. Duchesnay, *J. Mach. Learn. Res.* **2011**, *12*, 2825.
- [41] J. R. Quinlan, *Mach. Learn.* **1986**, *1*, 81.
- [42] H. Edelsbrunner, E. P. Mücke, *ACM Trans. Graphics (TOG)* **1994**, *13*, 43.
- [43] B. Delaunay, *Izv. Akad. Nauk SSSR* **1934**, *7*, 793.
- [44] A. Stukowski, *JOM* **2014**, *66*, 399.
- [45] L. Breiman, J. H. Friedman, R. A. Olshen, C. J. Stone, *Classification and Regression Trees*, Routledge, New York, USA **2017**.
- [46] O. V. Kharissova, B. I. Kharisov, *RSC Adv.* **2014**, *4*, 30807.
- [47] B. Bhattarai, P. Biswas, R. Atta-Fynn, D. A. Drabold, *Phys. Chem. Chem. Phys.* **2018**, *20*, 19546.
- [48] S. V. King, *Nature* **1967**, *213*, 1112.
- [49] J. H. Lehman, M. Terrones, E. Mansfield, K. E. Hurst, V. Meunier, *Carbon* **2011**, *49*, 2581.
- [50] J. Xiao, J. Staniszewski, J. Gillespie Jr, *Mater. Sci. Eng. A* **2010**, *527*, 715.
- [51] T. Fujimori, L. R. Radovic, A. B. Silva-Tapia, M. Endo, K. Kaneko, *Carbon* **2012**, *50*, 3274.
- [52] T. M. Lusk, T. D. Wu, D. L. Carr, *Phys. Rev. B* **2010**, *81*, 155444.
- [53] P. A. Throver, in *Chemistry and Physics of Carbon* (Ed: P. L. Walker Jr.), vol. 5, Marcel Dekker, New York **1969**, pp. 217–320.
- [54] A. Stone, D. Wales, *Chem. Phys. Lett.* **1986**, *128*, 501.
- [55] S. G. Louie, *Electronic Properties, Junctions, and Defects of Carbon Nanotubes*, Springer Berlin Heidelberg, Berlin, Heidelberg **2001**, pp. 113–145.
- [56] J. Mintmire, C. White, *Carbon* **1995**, *33*, 893.
- [57] K. Prasai, K. N. Subedi, K. Ferris, P. Biswas, D. A. Drabold, *Phys. Status Solidi RRL* **2018**, *12*, 1800238.
- [58] K. N. Subedi, K. Prasai, D. A. Drabold, *Phys. Status Solidi B* **2021**, *258*, 2000438.
- [59] G. Dresselhaus, M. S. Dresselhaus, R. Saito, *Physical Properties of Carbon Nanotubes*, World Scientific, Singapore **1998**.
- [60] A. Lekawa-Raus, J. Patmore, L. Kurzepa, J. Bulmer, K. Koziol, *Adv. Funct. Mater.* **2014**, *24*, 3661.
- [61] P. A. Sundqvist, F. J. Garcia-Vidal, F. Flores, *Phys. Rev. B* **2008**, *78*, 205427.
- [62] M. S. Purewal, B. H. Hong, A. Ravi, B. Chandra, J. Hone, P. Kim, *Phys. Rev. Lett.* **2007**, *98*, 186808.
- [63] C. T. White, T. N. Todorov, *Nature* **1998**, *393*, 240.

- [64] D.-K. Lee, J. Yoo, H. Kim, B.-H. Kang, S.-H. Park, *Materials* **2022**, *15*, 1356.
- [65] S. Reich, C. Thomsen, J. Maultzsch, *Carbon Nanotubes: Basic Concepts and Physical Properties*, John Wiley & Sons, New York, NY **2004**.
- [66] W. Fa, J. Chen, J. Dong, *Eur. Phys. J. B* **2004**, *37*, 473.
- [67] P. Lambin, C. R. *Phys.* **2003**, *4*, 1009.
- [68] D.-I. Moon, A. Rukhin, R. P. Gandhiraman, B. Kim, S. Kim, M.-L. Seol, K. J. Yoon, D. Lee, J. Koehne, J.-W. Han, M. Meyyappan, *ACS Appl. Electron. Mater.* **2019**, *1*, 1162.
- [69] M. Kozicki, US17/112,668, **2021**.
- [70] C. Ugwumadu, K. N. Subedi, R. Thapa, P. Apsangi, S. Swain, M. N. Kozicki, D. A. Drabold, *J. Non-Cryst. Solids: X* **2022**, Unpublished.
- [71] S. Behnia, F. Rahimi, *Phys. Lett. A* **2018**, *382*, 3274.
- [72] Y. Wang, G. J. Weng, *Electrical Conductivity of Carbon Nanotube- and Graphene-based Nanocomposites*, Springer International Publishing, Cham, **2018**, pp. 123–156.
- [73] O. Schmidt, *Z. Phys. Chem.* **1940**, *47*, 1.
- [74] F. Rozploch, J. Patyk, J. Stankowski, *Acta Phys. Pol. A* **2007**, *112*, 557.
- [75] F. Rozploch, J. Patyk, P. Szroeder, *Mol. Phys. Rep.* **2003**, *37*, 24.
- [76] S. Grimme, J. Antony, S. Ehrlich, H. Krieg, *J. Chem. Phys.* **2010**, *132*, 154104.
- [77] M. S. Dresselhaus, A. Jorio, A. G. Souza Filho, R. Saito, *Philos. Trans. R. Soc. A* **2010**, *368*, 5355.
- [78] R. Saito, M. Hofmann, G. Dresselhaus, A. Jorio, M. S. Dresselhaus, *Adv. Phys.* **2011**, *60*, 413.
- [79] A. C. Ferrari, J. Robertson, *Phys. Rev. B* **2000**, *61*, 14095.
- [80] J. Kastner, T. Pichler, H. Kuzmany, S. Curran, W. Blau, D. Weldon, M. Delamesiere, S. Draper, H. Zandbergen, *Chem. Phys. Lett.* **1994**, *221*, 53.
- [81] K. Sbai, A. Rahmani, H. Chadli, J.-L. Bantignies, P. Hermet, J.-L. Sauvajol, *J. Phys. Chem. B* **2006**, *110*, 12388.
- [82] Á. I. López-Lorente, B. Mizaikoff, *TrAC Trends Anal. Chem.* **2016**, *84*, 97.
- [83] H. R. Seyf, L. Yates, T. L. Bougher, S. Graham, T. D. Baratunde, A. Cola, M.-H. Ji, J. Kim, R. Dupuis, W. Lv, A. Henry, *npj Comput. Mater.* **2017**, *3*, 49.
- [84] P. B. Allen, J. L. Feldman, *Phys. Rev. B* **1993**, *48*, 12581.
- [85] P. B. Allen, J. L. Feldman, J. Fabian, F. Wooten, *Philos. Mag. B* **1999**, *79*, 1715.
- [86] R. J. Bell, D. C. Hibbins-Butler, *J. Phys. C: Solid State Phys.* **1975**, *8*, 787.
- [87] J. L. Feldman, P. B. Allen, S. R. Bickham, *Phys. Rev. B* **1999**, *59*, 3551.
- [88] M. S. Dresselhaus, G. Dresselhaus, R. Saito, A. Jorio, *Phys. Rep.* **2005**, *409*, 47.
- [89] X. Zhao, Y. Ando, L.-C. Qin, H. Kataura, Y. Maniwa, R. Saito, *Chem. Phys. Lett.* **2002**, *361*, 169.
- [90] H. Jantoljak, J.-P. Salvetat, L. Forro, C. Thomsen, *Appl. Phys. A: Mater. Sci. Process.* **1998**, *67*, 113.
- [91] C. Miao, H. Li, W. Guo, *Sci. China Phys. Mech. Astron.* **2012**, *55*, 940.
- [92] P. G. Klemens, *J. Wide Bandgap Mater.* **2000**, *7*, 332.
- [93] D. Surblys, H. Matsubara, G. Kikugawa, T. Ohara, *J. Appl. Phys.* **2021**, *130*, 215104.
- [94] D. Surblys, H. Matsubara, G. Kikugawa, T. Ohara, *Phys. Rev. E* **2019**, *99*, 051301.
- [95] M. S. Green, *J. Chem. Phys.* **1954**, *22*, 398.
- [96] R. Kubo, M. Yokota, S. Nakajima, *J. Phys. Soc. Jpn.* **1957**, *12*, 1203.
- [97] S. Nosé, *Mol. Phys.* **1984**, *52*, 255.
- [98] W. G. Hoover, *Phys. Rev. A* **1985**, *31*, 1695.
- [99] Z. Han, A. Fina, *Prog. Polym. Sci.* **2011**, *36*, 914.
- [100] P. Kim, L. Shi, A. Majumdar, P. L. McEuen, *Phys. Rev. Lett.* **2001**, *87*, 215502.
- [101] R. Franz, G. Wiedemann, *Ann. Phys. (Leipzig)* **1853**, *165*, 497.